Contents

Contents

- Neutron stars are one type of **compact remnant**, created during the final stages of stellar evolution.

- When a massive star of $\sim 8 - 30\,M_\odot$ runs out of fuel, it collapses under its own gravitational attraction and explodes in a **supernova**.

- During collapse, **electron captures** $(p + e^- \to n + \nu_e)$ produce neutrons.

- They have radii between $9 - 15\,\mathrm{km}$ and weigh $1.2 - 2\,M_\odot$, resulting in densities up to $\rho \simeq 10^{15}\,\mathrm{g\,cm^{-3}}$.
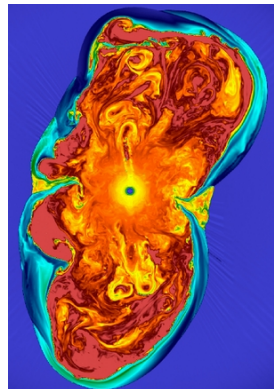

Figure 1: Snapshot of 3D core-collapse supernova simulation (Mösta et al., 2014).

- The interior structure is complex and influenced by the (unknown) equation of state. However, there is a **canonical understanding**.

- After $\sim 10^4$ years neutron stars are in equilibrium and have temperatures of $10^6 - 10^8$ K. They are composed of **distinct layers**.

- For our purposes we separate neutron stars into a **solid crust** and a **fluid core**, containing three distinct superfluid components.
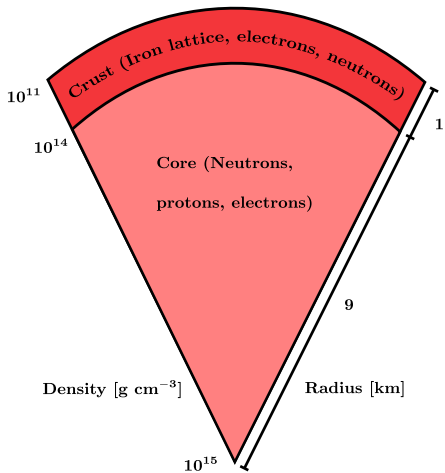

Figure 2: Sketch of the neutron star interior.

- Neutron stars are hot compared to low-temperature experiments on Earth, but cold in terms of their nuclear physics (Migdal, 1959).

- Neutrons and protons are **fermions** that can become unstable to **Cooper pair** formation due to an attractive contribution to the nucleon-nucleon interaction potential.

- Pairing process is described within the standard microscopic **BCS** theory of superconductivity (Bardeen, Cooper & Schrieffer, 1957).

- Compare the equilibrium to the nucleons' **Fermi temperature**:

$$T_{\mathrm{F}} = k_{\mathrm{B}}^{-1} E_{\mathrm{F}} \sim 10^{12}\,\mathrm{K} \gg 10^{6} - 10^{8}\,\mathrm{K}. \tag{1}$$

Neutron star matter is strongly influenced by quantum mechanics!

- Detailed BCS calculations provide the pairing gaps Δ, which are associated with the **critical temperatures** T_c for the superfluid and superconducting phase transitions.
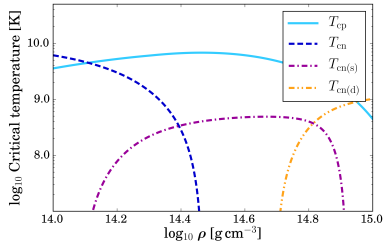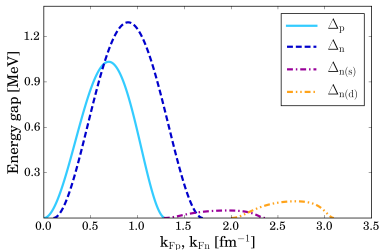

Figure 3: Left: Parametrised proton (singlet) and neutron (singlet, triplet) energy gaps as a function of Fermi wave numbers (Ho, Glampedakis & Andersson, 2012). Right: Critical temperatures of superconductivity/superfluidity as a function of the neutron star density. The values are computed for the NRAPR equation of state (Steiner et al., 2005; Chamel, 2008).

Contents

- Superfluids flow **without viscosity**, while superconductors have vanishing electrical conductivity and exhibit **Meissner effect**.

- Both states involve large numbers of particles condensed into the same quantum state, characteristic for **macroscopic quantum phenomena**.

- Most of our understanding of superfluidity and superconductivity in neutron stars originates from **laboratory counterparts**.
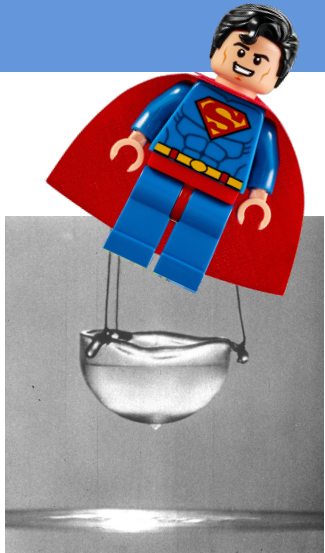
Figure 4: Superfluid helium creeps up the walls to eventually empty the bucket.

- The superfluids can be characterised by **macroscopic wave functions** $\Psi = \Psi_0\, e^{i\varphi}$ that satisfy the Schrödinger equation. Using the standard formalism one can determine a **superfluid velocity**

$$\boldsymbol{v}_{\mathsf{S}} \equiv \frac{\boldsymbol{j}_{\mathsf{S}}}{\rho_{\mathsf{S}}} = \frac{\hbar}{m_{\mathrm{c}}}\,\nabla\varphi, \qquad \Rightarrow \qquad \boldsymbol{\omega} \equiv \nabla \times \boldsymbol{v}_{\mathsf{S}} = 0. \qquad (2)$$

Figure 5: Envisage vortices as tiny, rotating tornadoes.

- Superflow is **irrotational**: the superfluids can only rotate by forming a **regular vortex array**.

- Each vortex carries a **quantum of circulation** $\kappa = h/2m \approx 2.0 \times 10^{-3}\,\mathrm{cm^2\,s^{-1}}$ and has a size

$$\xi_{\mathrm{v}} \approx 1.5 \times 10^{-11}\,(1 - x_{\mathrm{p}})^{1/3}\left(\frac{m}{m_{\mathrm{n}}^*}\right)\rho_{14}^{1/3}\left(\frac{10^9\,\mathrm{K}}{T_{\mathrm{cn}}}\right)\mathrm{cm}. \qquad (3)$$

■ The vortices arrange themselves in a **hexagonal array** (Abrikosov, 1957) and their circulation mimics solid-body rotation on large scales. The **averaged vorticity** and **vortex area density** are given by

$$\boldsymbol{\omega} = 2\boldsymbol{\Omega} = \mathcal{N}_{\mathrm{v}}\kappa\hat{\boldsymbol{z}}, \qquad \mathcal{N}_{\mathrm{v}} \approx 6.3 \times 10^5 \left(\frac{10\,\mathrm{ms}}{P}\right)\mathrm{cm}^{-2}. \qquad (4)$$

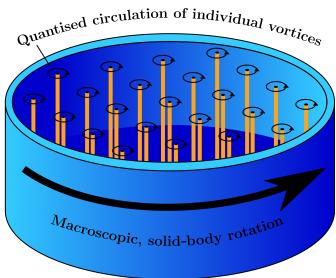Quantised circulation of individual vortices

Macroscopic, solid-body rotation

Figure 6: Vortex array of a rotating superfluid mimics solid-body rotation.

■ For a regular array, the **intervortex distance** is given by $d_{\mathrm{v}} \simeq \mathcal{N}_{\mathrm{v}}^{-1/2}$:

$$d_{\mathrm{v}} \approx 1.3 \times 10^{-3} \left(\frac{P}{10\,\mathrm{ms}}\right)^{1/2}\mathrm{cm}. \qquad (5)$$

A change in angular momentum is achieved by creating (spin-up) or destroying (spin-down) vortices.

- The vortices interact with the viscous fluid component causing dissipation. This **mutual friction** influences laboratory systems (Hall & Vinen, 1956) and neutron stars (Alpar, Langer & Sauls, 1984).

- Taking $\boldsymbol{\Omega} = \Omega\hat{\boldsymbol{\Omega}}$, the **vortex-averaged** drag force in the core is

$$\boldsymbol{F}_{\mathrm{mf}} = 2\mathcal{B}\rho_{\mathrm{n}}\hat{\boldsymbol{\Omega}} \times [\boldsymbol{\Omega} \times (\boldsymbol{v}_{\mathrm{n}} - \boldsymbol{v}_{\mathrm{e}})] + 2\mathcal{B}'\rho_{\mathrm{n}}\boldsymbol{\Omega} \times (\boldsymbol{v}_{\mathrm{n}} - \boldsymbol{v}_{\mathrm{e}}). \qquad (6)$$

- The **dimensionless parameters** $\mathcal{B}$ and $\mathcal{B}'$ reflect the strength of $\boldsymbol{F}_{\mathrm{mf}}$. They are calculated by considering mesoscopic **coupling physics** for a single vortex and then averaging for the full array.

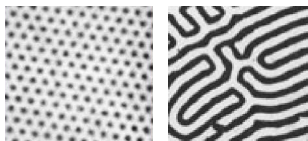**There are large uncertainties in calculating mutual friction coefficients, which differ between the crust and the core.**

Figure 7: Superconducting states.

■ Due to high conductivity, the magnetic flux cannot be expelled from their interiors ⇒ neutron stars do not exhibit Meissner effect and are in a **metastable** state (Baym, Pethick & Pines, 1969; Ho, Andersson & Graber, 2017).

■ The exact phase depends on the **characteristic lengthscales** involved:

$$\kappa = \frac{\lambda}{\xi_{\mathrm{ft}}} \approx 3 \left(\frac{m_{\mathrm{p}}^*}{m} \right)^{3/2} \rho_{14}^{5/6} \left(\frac{x_{\mathrm{p}}}{0.05} \right)^{5/6} \left(\frac{T_{\mathrm{cp}}}{10^9 \, \mathrm{K}} \right) > \frac{1}{\sqrt{2}}. \tag{7}$$

■ Estimates predict a **type-II state** in the outer core with

$$H_{\mathrm{c1}} = \frac{4\pi \mathcal{E}_{\mathrm{ft}}}{\phi_0} \approx 1.9 \times 10^{14} \left(\frac{m}{m_{\mathrm{p}}^*} \right) \rho_{14} \left(\frac{x_{\mathrm{p}}}{0.05} \right) \mathrm{G}, \tag{8}$$

$$H_{\mathrm{c2}} = \frac{\phi_0}{2\pi \xi_{\mathrm{ft}}^2} \approx 2.1 \times 10^{15} \left(\frac{m_{\mathrm{p}}^*}{m} \right)^2 \rho_{14}^{2/3} \left(\frac{x_{\mathrm{p}}}{0.05} \right)^{2/3} \left(\frac{T_{\mathrm{cp}}}{10^9 \, \mathrm{K}} \right)^2 \mathrm{G}. \tag{9}$$

- Each fluxtube carries a **flux quantum** $\phi_0 = hc/2e \approx 2.1 \times 10^{-7} \,\mathrm{G\,cm^2}$ and has a size

$$\xi_{\mathrm{ft}} \approx 3.9 \times 10^{-12} \left(\frac{m}{m_{\mathrm{p}}^*}\right) \rho_{14}^{1/3} \left(\frac{x_{\mathrm{p}}}{0.05}\right)^{1/3} \left(\frac{10^9\,\mathrm{K}}{T_{\mathrm{cp}}}\right) \,\mathrm{cm}. \qquad (10)$$

- All flux quanta add up to the total magnetic flux. The **averaged magnetic induction** is related to the fluxtube area density $\mathcal{N}_{\mathrm{ft}}$:

$$B = \mathcal{N}_{\mathrm{ft}}\phi_0, \quad \to \quad \mathcal{N}_{\mathrm{ft}} \approx 4.8 \times 10^{18} \left(\frac{B}{10^{12}\,\mathrm{G}}\right) \,\mathrm{cm^{-2}}. \qquad (11)$$

- The typical **interfluxtube distance** is given by $d_{\mathrm{ft}} \simeq \mathcal{N}_{\mathrm{ft}}^{-1/2}$ with

$$d_{\mathrm{ft}} \approx 4.6 \times 10^{-10} \left(\frac{B}{10^{12}\,\mathrm{G}}\right)^{-1/2} \,\mathrm{cm}. \qquad (12)$$

- **Field evolution** is related to the mechanisms affecting fluxtube motion (Muslimov & Tsygan, 1985; Graber et al., 2015; Graber, 2017, e.g.).

- Macroscopic **Euler equations** for superfluid neutrons and charged fluid in zero-temperature limit (Glampedakis, Andersson & Samuelsson, 2011)

$$\left(\partial_t + v_{\mathrm{n}}^j \nabla_j\right)\left[v_{\mathrm{n}}^i + \varepsilon_{\mathrm{n}} w_{\mathrm{np}}^i\right] + \nabla^i \tilde{\Phi}_{\mathrm{n}} + \varepsilon_{\mathrm{n}} w_{\mathrm{pn}}^j \nabla^i v_j^{\mathrm{n}} = f_{\mathrm{mf}}^i + f_{\mathrm{mag,n}}^i, \qquad (13)$$

$$\left(\partial_t + v_{\mathrm{p}}^j \nabla_j\right)\left[v_{\mathrm{p}}^i + \varepsilon_{\mathrm{p}} w_{\mathrm{pn}}^i\right] + \nabla^i \tilde{\Phi}_{\mathrm{p}} + \varepsilon_{\mathrm{p}} w_{\mathrm{np}}^j \nabla^i v_j^{\mathrm{p}} = -\frac{n_{\mathrm{n}}}{n_{\mathrm{p}}} f_{\mathrm{mf}}^i + f_{\mathrm{mag,p}}^i, \quad (14)$$

with $w_{\mathrm{xy}}^i \equiv v_{\mathrm{x}}^i - v_{\mathrm{y}}^i$. Modified by **new force terms**, f_{mf}^i and $f_{\mathrm{mag,x}}^i$, due to vortices/fluxtubes and **entrainment**, ε_{x} (Andreev & Bashkin, 1975).

- Supplemented by **continuity equations** and **Poisson's equation**,

$$\partial_t n_{\mathrm{x}} + \nabla_i(n_{\mathrm{x}} v_{\mathrm{x}}^i) = 0, \qquad \nabla^2 \Phi = 4\pi G \rho, \qquad (15)$$

and an evolution equation for the magnetic induction B.

Contents

- **Glitches** are sudden spin-ups caused by angular momentum transfer from a crustal superfluid, decoupled from the lattice (and everything tightly coupled) due to vortex pinning (Anderson & Itoh, 1975).
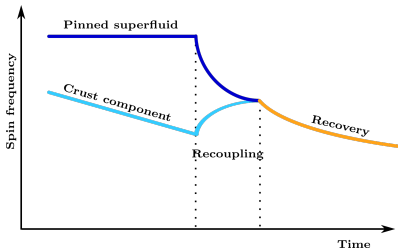

Figure 8: Sketch of an idealised glitch.

- Catastrophic vortex unpinning triggers the glitch and frictional forces acting on **free vortices** govern the **neutron star's post-glitch response**.

- Observations suggest that the **crust spin-up** after a glitch is very fast (Dodson, Lewis & McCulloch, 2007; Palfreyman et al., 2018).

- Within **hydrodynamical models**, the recoupling is captured via the **mutual friction** coefficient $\mathcal{B}$, directly connected to **microphysics**.

- Decompose the star into **crust superfluid**, **core superfluid** and a non-superfluid **'crust' component**. The latter two rotate rigidly and are coupled via a constant mutual friction $\mathcal{B}_{\mathrm{core}} \approx 5 \times 10^{-5}$.

- Neglecting entrainment for simplicity, the **equations of motion** are

$$\dot{\Omega}_{\mathrm{sf}} = \mathcal{B}\left[2\Omega_{\mathrm{sf}} + \tilde{r}\,\frac{\partial\Omega_{\mathrm{sf}}}{\partial\tilde{r}}\right](\Omega_{\mathrm{crust}} - \Omega_{\mathrm{sf}}), \qquad (16)$$

$$\dot{\Omega}_{\mathrm{core}} = 2\mathcal{B}_{\mathrm{core}}\Omega_{\mathrm{core}}\,(\Omega_{\mathrm{crust}} - \Omega_{\mathrm{core}}), \qquad (17)$$

$$\dot{\Omega}_{\mathrm{crust}} = -\frac{N_{\mathrm{ext}}}{I_{\mathrm{crust}}} - \frac{I_{\mathrm{core}}}{I_{\mathrm{crust}}}\,\dot{\Omega}_{\mathrm{core}} - \frac{1}{I_{\mathrm{crust}}}\int \rho\tilde{r}^2\dot{\Omega}_{\mathrm{sf}}\,\mathrm{d}V. \qquad (18)$$

- We calculate the coupling $\mathcal{B}(\tilde{r})$ in the crust for realistic microphysics and integrate Eqs. (16)-(18) in cylindrical geometry for typical **Vela pulsar** parameters ($\Omega_{\mathrm{crust}}(0) \approx 70\,\mathrm{Hz}$, $\Delta\Omega_{\mathrm{crit}} \approx 10^{-2}\,\mathrm{Hz}$) for $120\,\mathrm{s}$.
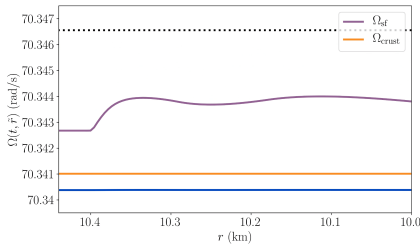
Figure 9: Evolution in the inner crust for model (A).

■ The superfluid rotates **differentially** due to $\mathcal{B}(\tilde{r})$-dependence. Eventually, it has transferred all excess angular momentum to the crust and spun down to a **new steady state**, where all three components corotate.
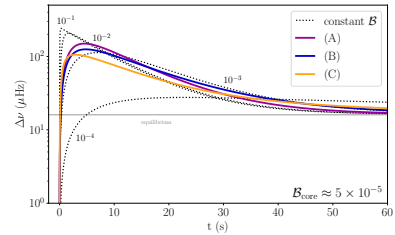
■ Computing the change in (observed) crust frequency $\Delta\nu$ shows that the glitch shape depends crucially on the **relative strength** between the crust and core mutual friction.

Figure 10: Change in crustal frequency with time.

- First single-pulse observations of a glitch in the Vela pulsar (Palfreyman et al., 2018) allow a **comparison** between the data and our predictions.
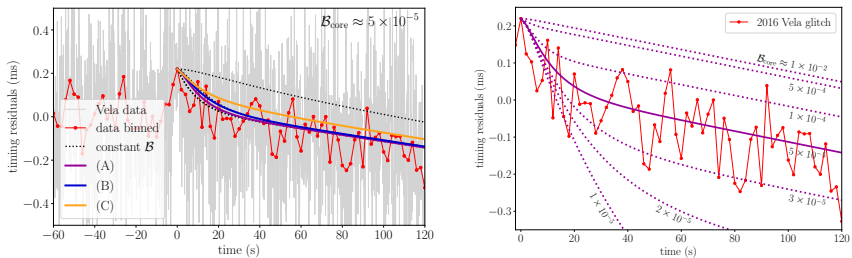
Figure 11: Comparison between theoretical timing residuals and observations of the 2016 Vela glitch.

The shape is almost insensitive to the crustal profile as long as $\mathcal{B} \gtrsim 10^{-3}$ but very sensitive to the core coupling. The data suggests a narrow range $3 \times 10^{-5} \lesssim \mathcal{B}_{core} \lesssim 10^{-4} \Rightarrow$ test that!!

Contents

- The neutron star interior contains at least three distinct superfluid components and theoretical modelling of their behaviour is very difficult $\Rightarrow$ use **laboratory counterparts** to understand them better.

- It is **not possible to replicate** the extreme conditions present in neutron stars. However, we could use known laboratory analogues that are easy to manipulate to recreate and **study specific** neutron star characteristics.

- I will focus on a few promising examples. For more details see Graber, Andersson & Hogg (2017).
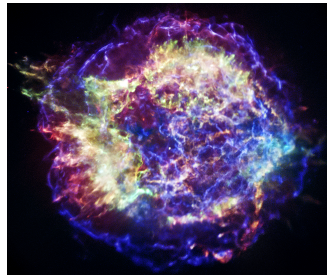
Figure 12: Chandra X-ray observation of the Cassiopeia A supernova remnant.
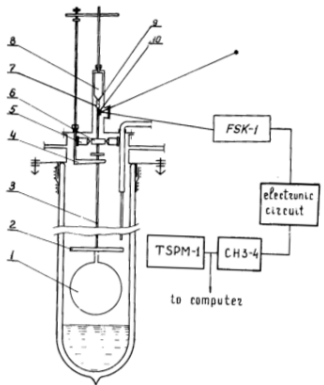
Figure 13: Schematic setup of the helium II spin-up experiments (Tsakadze & Tsakadze, 1980).

- First (and only) **systematic analysis** of rotating helium II by Tsakadze & Tsakadze (1980), shortly after first observations of **glitches** in the Vela and Crab pulsar.

- Validate presence of superfluid components in neutron stars by measuring **relaxation timescales** after initial changes in the container's rotation.

- Performed for various temperatures, vessel configurations and rotational properties.

- Model comparison is hard (Reisenegger, 1993; van Eysden & Melatos, 2011).
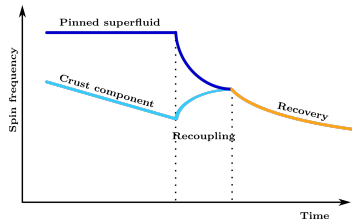
Figure 14: Sketch of an idealised neutron star glitch.
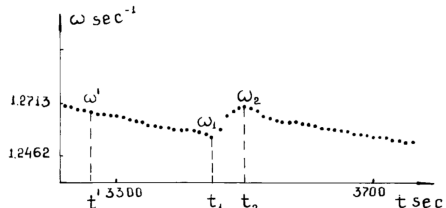
Figure 15: Measurement of a laboratory glitch.

- **Glitches** are not only detected in neutron stars, but have also been observed in laboratory helium experiments. This supports the idea that they are caused by an **internal superfluid reservoir**.

- There is **only one (!!)** observation of a helium II glitch. Updated experiments could help to understand aspects such as the trigger.

- Helium-3 becomes superfluid below 3 mK. The transition is different to bosonic helium II because helium-3 atoms are fermions and have to form **Cooper-pairs** as expected for the neutron star interior.

- The pairing occurs in a spin-triplet, *p*-wave state: the Cooper pairs have internal structure resulting in **3 superfluid phases** (Vollhardt, 1998).

- The **B-phase** behaves similar to helium II or the crustal neutron superfluid. The **A-phase** exhibits anisotropic behaviour and resembles the core neutron superfluid.
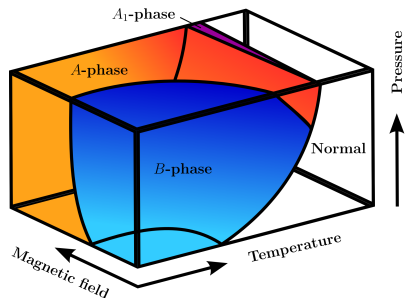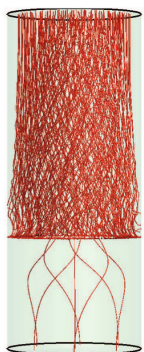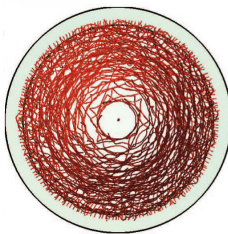

Figure 16: Schematic phase diagram of helium-3.

- It is not understood how **interfaces** influence the neutron star dynamics ⇒ **crust-core transition** between two superfluids??

Figure 17: Vortex-line simulation for spin-down of two-phase helium-3 (Walmsley et al., 2011).

- Study vortices across an interface with rotating **two-phase samples** (different $\mathcal{B}$, $\mathcal{B}'$) using NMR measurements and modern vortex-line simulations (Walmsley et al., 2011).

- Interface strongly modifies dynamics:
  - ▸ **Vortex sheet** formation
  - ▸ **Vortex tangle** forms in B-phase, reconnections increase dissipation
  - ▸ **Differential rotation**

- Interface can become unstable to Kelvin-Helmholtz instability (Finne et al., 2006).

- A BEC of **weakly-interacting bosons** was first realised by cooling Rubidium atoms to $T \sim$ nK (Anderson et al., 1995; Davis et al., 1995), and the superfluid transition observed shortly after (Matthews et al., 1999; Madison et al., 2000).

- Although the field is relatively young, ultra-cold gases provide **many possibilities** to study superfluidity: e.g. fermionic gases, two-component systems, optical lattices, etc.

- Very simple advantage: **absorption imaging** of clouds is a great tool to study behaviour of individual vortices.
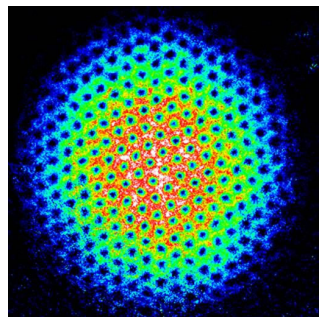

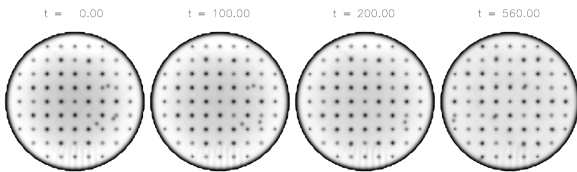Figure 18: Vortex array in a rotating, dilute BEC of Rubidium atoms (Engels et al., 2002).

Figure 19: Snapshots of superfluid density during the spin-down of a BEC (Warszawski & Melatos, 2012).

- Time evolution of the **Gross-Pitaevskii equation** describes vortex motion $\Rightarrow$ use this approach to study the pinned **crustal superfluid** in neutron stars (Warszawski & Melatos, 2012).

- Collective vortex motion in the presence of pinning potential can cause **glitch-like events** $\Rightarrow$ study the unknown trigger and glitch statistics.

- **Two-component GP** formalisms have been used to study neutron star core properties (Alford & Good, 2008; Drummond & Melatos, 2017, e.g.).
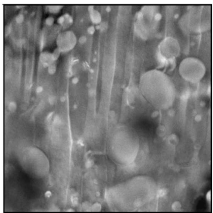
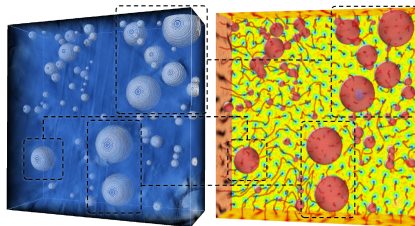**Figure 20:** 3D STEM tomogram with ~ 70 pinning sites (Ortalan et al., 2009).

Figure 21: Modelled fluxtube motion. Colour reflects order parameter (Sadovskyy et al., 2016).

- Experimental data and modern calculations complement each other: Determine **fluxtube motion** in a **realistic pinning landscape** by numerically solving time-dependent Ginzburg-Landau equations.

- Account for pinning defects, fluxtube flexibility, long-range fluxtube repulsion, fluxtube cutting and reconnections.
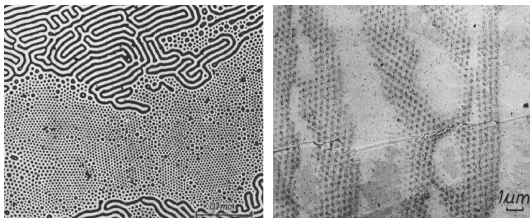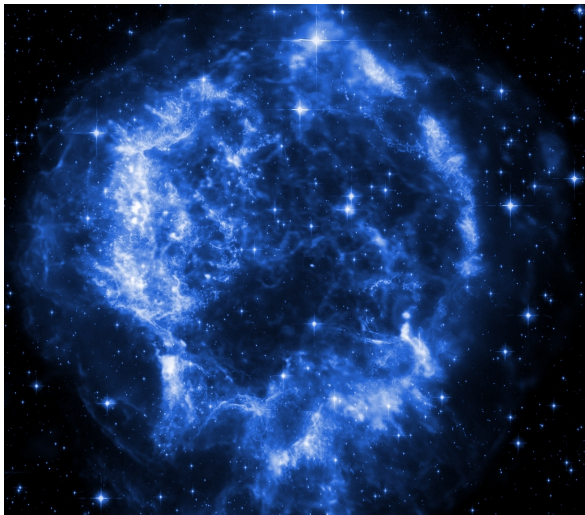
Figure 22: Intermediate state of type-I and type-II phases (Brandt & Essmann, 1987; Essmann, 1971).

- Our understanding of **macroscopic superconductivity** in neutron stars is based on time-independent equilibrium considerations. It is unclear what happens in detail as the star cools below T_c.

- Experiments could help to better understand the **microphysical dynamics** of the superconducting phase transition and the resulting flux distribution $\Rightarrow$ how does the magnetic field actually look like?

Conclusions

- Neutron stars are expected to contain (at least) **three distinct quantum condensates** that influence the stars' macroscopic behaviour. The majority of our knowledge of these superfluids originates from theoretical work on their laboratory counterparts.

- Neutron star **glitches** are a direct manifestation of macroscopic superfluidity. Analysing observations of the post-glitch response provides information about the underlying **microphysics**.

- As significant progress has been made in understanding laboratory condensates, there are many exciting ways to **combine both fields** of research and probe the dynamics of the neutron star interior with superfluid/superconducting experiments.

■ We use the **crustal composition** of Negele & Vautherin (1973) and pinning **interaction parameters** from Epstein & Baym (1992) and Donati & Pizzochero (2006) to calculate $\mathcal{B}$ in the inner crust.

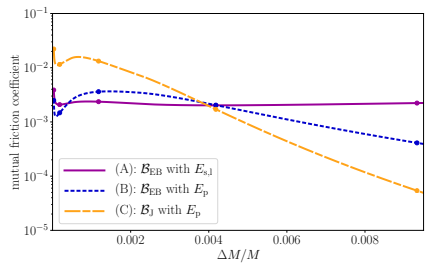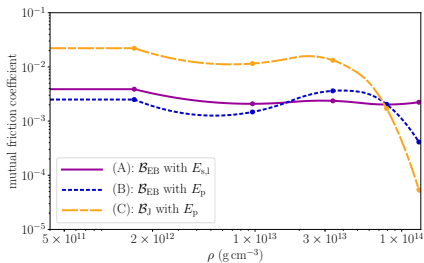■ The **bottom of the crust** carries the majority of the crustal mass.

Figure 23: Mutual friction strength for kelvin wave coupling (calculated Epstein & Baym (1992) and Jones (1992) according to as a function of (left) density and (right) relative overlying mass fraction.

■ Superfluidity and superconductivity are usually not accounted for in **gravitational wave signal** modelling as the effects of macroscopic condensates are generally believed to be negligible.

■ It has been suggested that **tidal disruption** during the late inspiral could dynamically couple to neutron star oscillations. If this is true than superfluidity/superconductivity could modify wave forms.
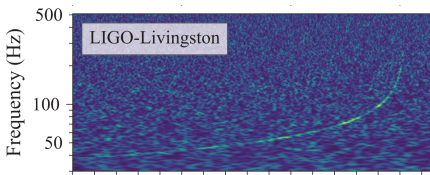

Figure 24: Time-frequency representation of GW170817 (Abbott et al., 2017).

■ Quantum states can only be present if stars are cold enough. Not clear how parameters like **temperature, conductivities and viscosities** evolve during the merger.

- Isolated neutron stars are likely to exhibit **non-spherical dynamical changes** in the interior fluid, which would result in the emission of gravitational waves (small amplitude).

- Interesting oscillations are the **r-modes** (inertial modes in rotating objects dominated by Coriolis force), because they are susceptible to the **CFS (Chandrasekhar-Friedman-Schutz) instability**.

- They can be prograde in inertial but retrograde in rotating frame, so that GW emission does not damp but increase amplitudes. Detailed physics will depend on presence of quantum condensates.
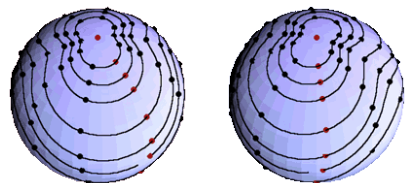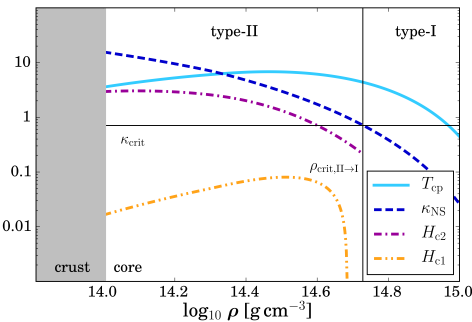

Figure 25: Oscillation seen by inertial (left) and rotating (right) observer (animation by Ben Owen).

Figure 26: Density-dependent parameters of NS superconductivity calculated for the NRAPR effective equation of state (Steiner et al., 2005). T_{cp} is obtained from Ho, Glampedakis & Andersson (2012).

■ Parameters of superconductivity are dependent on the neutron star density, i.e. the **equation of state**.

■ At higher densities one eventually has $\kappa < 1/\sqrt{2}$, so that the type-II state should transition into a **type-I state**. The critical density is

$$\rho_{\mathrm{crit,II\to I}} \approx 6.4 \times 10^{14} \left(\frac{m_{\mathrm{p}}^*}{m}\right)^{-\frac{9}{5}} \left(\frac{0.05}{x_{\mathrm{p}}}\right) \left(\frac{T_{\mathrm{cp}}}{10^9\,\mathrm{K}}\right)^{-\frac{6}{5}} \mathrm{g\,cm^{-3}}. \qquad (19)$$

Abbott B. P. et al., 2017, PhRvL, 119, 161101

Abrikosov A. A., 1957, JPCS, 2, 199

Alford M. G., Good G., 2008, PhRvB, 78, 024510

Alpar M. A., Langer S. A., Sauls J. A., 1984, ApJ, 282, 533

Anderson M. H., Ensher J. R., Matthews M. R., Wieman C. E., Cornell E. A., 1995, Sci, 269, 198

Anderson P. W., Itoh N., 1975, Natur, 256, 25

Andreev A. F., Bashkin E. P., 1975, JETP, 42, 164

Bardeen J., Cooper L. N., Schrieffer J. R., 1957, PhRv, 108, 1175

Baym G., Pethick C. J., Pines D., 1969, Natur, 224, 673

Brandt E. H., Essmann U., 1987, PSSBR, 144, 13

Chamel N., 2008, MNRAS, 388, 737

Davis K., Mewes M.-O., Andrews M. R., van Druten N. J., Durfee D. S., Kurn D. M., Ketterle W., 1995, PhRvL, 75, 3969

Dodson R., Lewis D., McCulloch P., 2007, Ap&SS, 308, 585

Donati P., Pizzochero P. M., 2006, PhLB, 640, 74

Drummond L. V., Melatos A., 2017, MNRAS, 472, 4851

Engels P., Coddington I., Haljan P. C., Cornell E. A., 2002, PhRvL, 89, 100403

Epstein R. I., Baym G., 1992, ApJ, 387, 276

Essmann U., 1971, Phy, 55, 83

Finne A. P., Eltsov V. B., Hänninen R., Kopnin N. B., Kopu J., Krusius M., Tsubota M., Volovik G. E., 2006, RPPh, 69, 3157

Graber V., 2017, AN, 338, 1

Graber V., Andersson N., Glampedakis K., Lander S. K., 2015, MNRAS, 453, 671

Graber V., Andersson N., Hogg M., 2017, IJMPD, 26, 1730015

Hall H. E., Vinen W. F., 1956, PSPSA, 238, 215

Ho W. C. G., Glampedakis K., Andersson N., 2012, MNRAS, 422, 2632

Ho W. W. C. G., Andersson N., Graber V., 2017, PhRvC, 96, 065801

Jones P. B., 1992, MNRAS, 257, 501

Madison K., Chevy F., Wohlleben W., Dalibard J., 2000, PhRvL, 84, 806

Matthews M. R., Anderson B. P., Haljan P. C., Hall D. S., Wieman C. E., Cornell E. A., 1999, PhRvL, 83, 2498

Migdal A. B., 1959, NucPh, 13, 655

Mösta P. et al., 2014, ApJ, 785, L29

Muslimov A. G., Tsygan A. I., 1985, SvA, 11, 80

Negele J. W., Vautherin D., 1973, NuPhA, 207, 298

Ortalan V., Herrera M., Rupich M. W., Browning N. D., 2009, PhyC, 469, 2052

Palfreyman J., Dickey J. M., Hotan A., Ellingsen S., van Straten W., 2018, Natur, 556, 219

Reisenegger A., 1993, JLTP, 92, 77

Sadovskyy I. A., Koshelev A. E., Glatz A., Ortalan V., Rupich M. W., Leroux M., 2016, PhRvP, 5, 014011

Steiner A. W., Prakash M., Lattimer J. M., Ellis P. J., 2005, PhR, 411, 325

Tsakadze J. S., Tsakadze S. J., 1980, JLTP, 39, 649

van Eysden C. A., Melatos A., 2011, JLTP, 165, 1

Vollhardt D., 1998, in Pair Correlations in Many-Fermion Systems, Kresin V. Z., ed., Springer US, Boston, MA, pp. 205–220

Walmsley P. M., Eltsov V. B., Heikkinen P. J., Hosio J. J., Hänninen R., Krusius M., 2011, PhRvB, 84, 184532